Bottlebrush Block Copolymer Thin Films

Zhan Chen[1], Xuchen Gan[1], Xindi Li[2], Mingqiu Hu[1], Yashodha Kahandawaarachchi[2], Hong-Gyu Seong[1], Todd Emrick[1], William T. Heller[3], Javid Rzayev[2], and Thomas P. Russell[1,4]**

[1]*Department of Polymer Science and Engineering, University of Massachusetts, Amherst, MA 01003*

[2]*Department of Chemistry, University at Buffalo, Buffalo, NY 14260*

[3] *Neutron Scattering Division, Oak Ridge National Laboratory, Oak Ridge, TN 37831*

[4]*Materials Sciences Division, Lawrence Berkeley National Laboratory, Berkeley, CA 37831*

Corresponding authors:

Javid Rzayev: jrzayev@buffalo.edu

Thomas P. Russell: russell@mail.pse.umass.edu

For Table of Contents Use Only

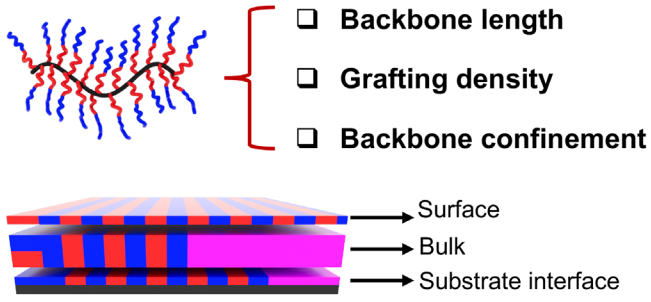

Depth-dependent morphology

Abstract

The self-assembly of block copolymers (BCPs) in thin films is governed by interfacial interactions (enthalpy) between the blocks and interfaces (at both the substrate and surface). Advantage can also be taken of entropy to control polymer orientation. Here, we synthesized a series of bottlebrush block copolymers (BBCPs), with deuterated polystyrene (DPS) as the core block and poly(solketal acrylate) (PSA) as the corona block, where the backbone length (N_{BB}) and grafting densities (GDs) were varied. The hydrophobic PSA block was converted to a hydrophilic poly(glyceryl acrylate) (PGA) block by solid-state hydrolysis, bringing the BBCP from a disordered into an ordered state with a lamellar microdomain morphology. The orientation of the morphology as a function of distance from the interfaces was systematically investigated by atomic force microscopy (AFM), interference microscopy, grazing-incidence small angle X-ray scattering (GISAXS), and grazing-incidence small angle neutron scattering (GISANS). For $N_{BB} = 1$ (diblock BCP), a mixed lamellar orientation was found. For $N_{BB} = 5$ (star-like BBCP), a vertical orientation of the lamellar microdomains was found dominantly at the interfaces that propagated into the bulk of the film, due to the entropic penalty associated with constraints on the junction points. Increasing the N_{BB} to 50 (rod-like BBCP) and 100 (worm-like BBCP) yielded a random orientation, as the side chains became overcrowded when aligned in the same direction. By reducing the grafting density (GD) of an $N_{BB} = 50$ BBCP from 100% to 75% and 50% by the incorporation of spacers into the backbone, the steric hindrance of side chains is reduced markedly, facilitating a vertical orientation of the lamellar microdomains. However, the vertical orientation becomes more random within the bulk of thin film for different BBCP architectures. By modifying the substrate with a layer of PS, the preferential interactions between the core block of the BBCP and the interfaces induce a reconfiguration of the BBCP, drawing the core block out to contact

substrate directly driven by enthalpy. Under these conditions, N_{BB} = 5 showed a predominantly parallel orientation of the lamellar microdomains, with the corona block minimizing contact with the substrate. Higher N_{BB} values of 50 and 100 showed more random orientation of the lamellar microdomains at different depths on the PS-modified substrate. Overall, thin film morphology was regulated by tuning the configuration of the BBCP, varying the entropic contribution to the microdomain orientation.

Keywords: Thin film, Block copolymers, Bottlebrush, Star, Architecture, Grazing-Incidence Small-Angle Neutron Scattering, Morphology

Introduction

The self-assembly of block copolymers (BCPs) offers a promising method to fabricate patterned templates with sub-10 nm full pitch, and an alternative to photolithographic methods that approach the diffraction limit.[1, 2] Key challenges and opportunities include the minimization of domain size and controlling the orientation of BCP microdomain morphology. To address domain size, a high χ-low N strategy has been proposed, where χ is the Flory-Huggins segmental interaction parameter between the two blocks, and N is the total number of BCP segments.[3] The periodicity of the microphase-separated domains (L_0) scales as $L_0 \approx \chi^{1/6} N^{2/3}$ and the segregation strength scales as χN.[4] Consequently, high χ-low N BCPs yield smaller domain sizes while maintaining a microphase separated morphology. The direct use of the high χ-low N strategy for thin film lithography faces several challenges, including the difficulty in finding a common solvent for both blocks, surface roughness after spin coating, and defects within the arrays of microdomains after thermal annealing, all arising from the strong immiscibility between the two blocks. To address these challenges, we describe a solid state transformation strategy using polystyrene-*block*-poly(solketal acrylate)/poly(solketal methacrylate) (PS-*b*-PSA/PSM), where the hydrophobic-hydrophobic BCP is cast from a single solvent to form a uniform thin film, followed by exposure to trifluoracetic acid (TFA) vapor, or a photoacid generation strategy to transform the hydrophobic PSA/PSM block into a hydrophilic poly(glycerol monoacrylate)/ poly(glycerol methacrylate) (PGA/PGM) block.[5-12] This significantly increases χ from 0.061 to 0.558 at 25 ℃ for PS-*b*-PSA and PS-*b*-PGA,[10] and from 0.035 to 0.438 at 25 ℃ for PS-*b*-PSM and PS-*b*-PGM,[11] respectively. Depending on N, the morphology of the BCP can be converted from the disordered state into a strongly microphase separated state.[10, 11]

Depending on the volume ratio between the two blocks, BCPs can self-assemble into well-defined morphologies as thin films, including spherical, cylindrical, gyroid and lamellar microdomain structures.[4] For nanofabrication, vertically oriented lamellae and cylinders are most desirable. However, for BCP thin films, the microdomains generally orient parallel to the substrate, due to preferential interactions of one block with the surface, e.g., the hydrophilic block preferring the polar silicon substrate, and/or differences in surface energies, e.g., the hydrophobic block preferring the air interface.[13] Previous efforts to orient BCP morphologies normal to the substrate focused on balancing enthalpic interactions. This includes balancing interfacial interactions with the substrate by anchoring a random copolymer to the substrate having a specific volume fraction of the segments comprising the BCP,[14] or by mediating interactions at the surface by annealing with a solvent that is miscible with both blocks.[3, 15, 16] In both cases, BCP orientation is dominated by enthalpic interactions. However, if the entropic penalty for maintaining parallel orientation exceeds the enthalpic gain, e.g., due to confinement, a normal BCP orientation can be achieved without surface modification. For instance, when the film thickness is incommensurate with the period of the BCP, the enthalpic preference of one block with the substrate or air surface can be overcome by the entropic penalty associated with stretching or compressing the BCP chains to maintain parallel orientation, resulting in microdomain orientation normal to the surface.[17]

The entropic contribution to the free energy can be amplified further by designing BCPs with advanced architectures.[18-21] The architectural design of bottlebrush block copolymers, including fine-tuning of backbone length and grafting density, ultimately leads to alteration of the polymer side chain and backbone configurations. For example, connecting multiple linear BCPs to a central backbone forms bottlebrush block copolymers (BBCPs). Depending on the ratio between the degree of polymerization of the backbone (N_{BB}) and side chains (N_{SC}), BBCPs can be categorized

into different regimes: (1) linear ($N_{BB} = 1$); (2) star-like ($N_{BB} << N_{SC}$); (3) rod-like ($N_{BB} \approx N_{SC}$); and (4) worm-like ($N_{BB} >> N_{SC}$).[22] As N_{BB} increases, the BBCP side chains become more densely packed and more constrained by the backbone, resulting in an increasingly stretched side chain conformation.[23-27] The reduced flexibility of the BBCP side chain increases the conformational-entropy penalty associated with a parallel orientation, which can override the enthalpic energy gain. Specifically, by assuming parallel orientation for BBCP to maximize the enthalpic energy gain, all side chains must align in the same direction, which will cause an overcrowded situation for side chains, especially near the backbone. To accommodate this steric hinderance, the side chains must further stretch at the cost of conformation entropy. As a result, BBCP may adopt a different orientation to lower the entropic penalty. For example, star BCPs can orient normal to the surface when entropy is the major driving force.[18-21] BBCPs, having multiple side chains attached to a backbone chain, offer greater opportunities to leverage entropy-driven polymer assembly.

The architecture-directed orientation can also vary depending on the depth within the thin film due to varying impact of surface interactions. For example, it has been reported that three-arm star BCPs with poly(dimethylsiloxane) (PDMS) as the core and PS as the corona adopt a parallel orientation near the air surface but vertical orientation near the substrate surface.[18] This is due to the significantly lower surface energy of the PDMS block compared to PS, while the polarity difference between the two blocks is relatively small. As a result, entropy dominates near the substrate surface, while enthalpy dominates near the air surface. Additionally, the surface interaction may also diminish within the bulk of the thin film. In the case of linear BCPs with a lamellar morphology, the parallel orientation propagates into the film, but the vertical orientation diminishes with increasing distance from both air and substrate interfaces.[8] The depth-dependent

morphology becomes more complicated when advanced architectures are utilized, as the entropic contribution to free energy also varies with depth.

In this work, we synthesized a series of symmetric BBCPs with deuterated polystyrene (DPS) as the core block and poly(solketal acrylate) (PSA) as the corona block by ruthenium benzylidene-initiated ring-opening metathesis polymerization (ROMP) of linear BCP macromonomers. When hydrolyzed by exposure to trifluoroacetic acid (TFA) vapor, the hydrophobic PSA block is converted to a hydrophilic poly(glycerol monoacrylate) (PGA) block, thereby transforming the BCP from a disordered state to a strongly microphase-separated state with a lamellar morphology. The self-assembled morphology was characterized by AFM, GISAXS, GISANS, and interference microscopy to reveal the morphologies at different depths, including near the air surface, in the bulk of the film, and near the substrate interface (**Scheme 1**). We systematically varied the degree of polymerization of the backbone (N_{BB}), the grafting density of the backbone (GD), and backbone confinement to vary the influence of entropy on the thin film morphologies. Controlling N_{BB} allowed the BBCP to transition across different configurational regimes, including linear, star-like, rod-like and worm-like structures. Adjusting the GD of side chains was achieved by incorporating phenyl-substituted norbornene units as spacers, thereby tuning configurational flexibility of the BCP side chains. By varying the substrate from hydrophilic (native SiO_x layer) to hydrophobic (modified with PS layer), the favorable surface interactions between the BBCP blocks and substrate shifted from the PGA corona block to the PS core block, which has a higher degree of confinement and more restricted mobility due to the direct bonding to the backbone, unlike the corona block, that is spatially separated from the backbone.[28, 29]

Results and Discussions

In this work, we synthesized a symmetric linear diblock macromonomer (MM) by sequential atom transfer radical polymerization (ATRP), with PSA as the corona block and norbornene-tethered DPS as the core block (**Figure 1**). Details of the syntheses were reported previously.[7, 8, 10, 12, 30] The degree of polymerization of the DPS and PSA blocks were found to be 30 and 44, respectively (details in **Supporting Information**). We first synthesized a series of densely grafted bottlebrush block copolymers (BBCPs) with different N_{BB} by ROMP of MMs. The resulting BBCPs are categorized by distinct shape regimes: (1) $N_{BB} = 1$: linear BCPs; (2) $N_{BB} = 5$: star-like BBCPs; (3) $N_{BB} = 25$: star-to-rod transition BBCPs; (4) $N_{BB} = 50$: rod-like BBCPs; and (5) $N_{BB} = 100$, worm-like BBCPs. At $N_{BB} = 50$, we varied the GD from 100% to 75% to 50% by copolymerization of NB-Ph with MM at fixed ratios.[24, 30] Comprehensive characterization details of the BBCPs are provided in **Table 1** and the **Supporting Information** (**Figure S1-S4**). Solid-state hydrolysis of hydrophobic PSA to hydrophilic PGA was achieved using TFA vapor.[5-9] This transformation changes the BBCP from hydrophobic-hydrophobic to hydrophilic-hydrophobic and drives the BBCP from the disordered state into the strongly microphase-separated state. In the bulk, all BBCPs with different N_{BB} and GD values showed lamellar morphologies after the solid state conversion, and the absence of the second-order reflection indicates equal thicknesses of the PS and PGA lamellar microdomains.[31] In **Figure S5**, we show Lorentz corrected SAXS data by plotting Iq^2 vs. q. We observed that increasing N_{BB} from 1 to 5 to 50 and to 100 at 100% GD reduced the d-spacing ($L_0 = 2\pi/q^*$) from 18.1 nm to 17.5 nm to 17.4 nm and to 17.2 nm, respectively. While increasing N_{BB} generally leads to an increase in the d-spacing, due to stretching of the side chains,[32] a reduction in the d-spacing at higher N_{BB} may be attributed to the large χ ($\chi = 0.558$) between the DPS and PGA blocks. Even in the linear regime, the chains are already highly stretched given the χ between PS and PGA reaching 0.558, and the bottlebrush architecture does

not cause additional stretching. Instead, the side chains may extend from the backbone chain in different directions to alleviate chain crowding and enable intermolecular interdigitation, where a greater degree of interdigitation at larger N_{BB} would reduce the d-spacing. A similar trend was observed for star BCPs with PS as the core and poly(2-vinylpyridine) (P2VP) as the corona, where higher arm numbers showed lower d-spacings. Additionally, decreasing GD from 100% to 75% to 50% at $N_{BB} = 50$ further reduced the d-spacing from 17.4 nm to 17.1 nm to 17.0 nm, since the side chain is forced to collapse to fill free space along the non-grafted portions of the backbone, leading to smaller d-spacings at lower GDs.

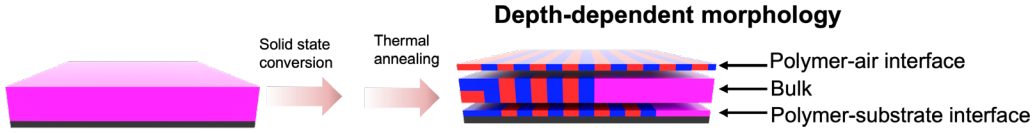

Scheme 1. Depth-dependent equilibrium morphology of $(DPS\text{-}b\text{-}PGA)_n$ BBCP thin films. Lamellae orientation may vary near the air surface, within the bulk, and near the substrate surface, after solid state conversion and thermal annealing of uniform $(DPS\text{-}b\text{-}PSA)_n$ thin film.

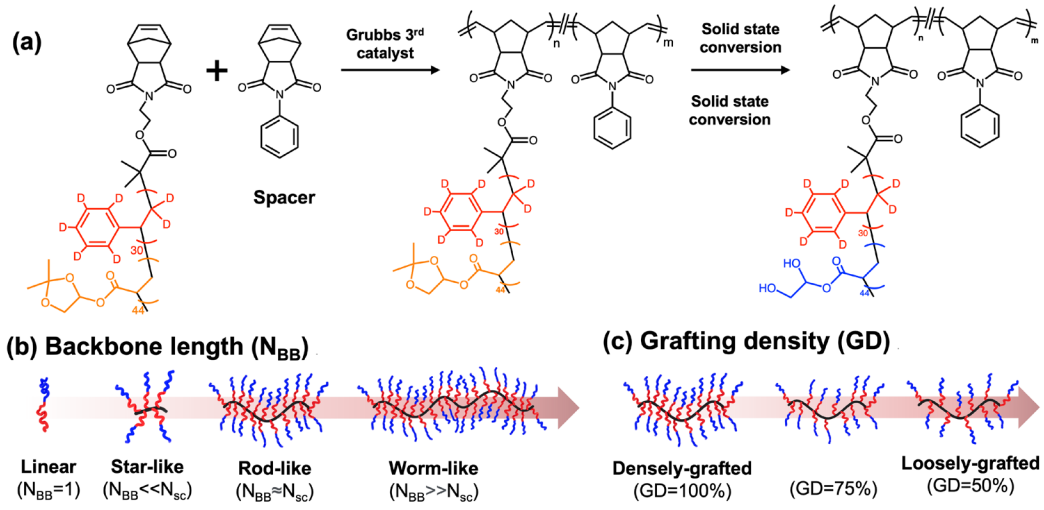

Figure 1. Synthesis of BBCP with linear, star-like, rod-like and worm-like configurations. (a) Synthetic route to prepare (DPS-*b*-PGA)$_n$ BBCP. Illustration of polymer shapes as a function of (b) N_{BB} and (c) GD.

Table 1. Characterization data of $(DPS\text{-}b\text{-}PSA)_{NBB\text{-}Grafting\ density\%}$

Sample[a]	N_{target} ([MMs]/[G3])	Graft density (%)	$M_{n,\ theo}$ (kDa)	$Đ^b$
$(DPS\text{-}b\text{-}PSA)_1$	1	100	12	1.37
$(DPS\text{-}b\text{-}PSA)_5$	5	100	58	1.15
$(DPS\text{-}b\text{-}PSA)_{25}$	25	100	290	1.14
$(DPS\text{-}b\text{-}PSA)_{50}$	50	100	579	1.16
$(DPS\text{-}b\text{-}PSA)_{50\text{-}75\%}$	38/12	75	442	1.16
$(DPS\text{-}b\text{-}PSA)_{50\text{-}50\%}$	25/25	50	295	1.13
$(DPS\text{-}PSA)_{100}$	100	100	1158	1.35

a. Samples without additional special notes of GD indicate 100% GD.

b. Polydispersity (*Đ)* was measured by SEC calibrated with PEG in DMF.

Effect of N_{BB} on BBCP thin film morphology

Uniform thin films of $(DPS\text{-}b\text{-}PSA)_n$, ~50 nm, were obtained by spin-coating from toluene solutions, followed by TFA-induced solid-state conversion and thermal annealing to reach an equilibrated lamellar morphology. Spin coating different $(DPS\text{-}b\text{-}PSA)_n$ samples at fixed solution concentration (12 mg/ml) in toluene and a constant spinning speed (2000 rpm) can efficiently yield uniform thin films with similar thicknesses and roughnesses. In-situ solid-state hydrolysis using TFA vapor effectively and cleanly converts the PSA blocks into PGA blocks without inducing dewetting or introducing additional artifacts. After hydrolysis, doing solvent vapor annealing for the resulting amphiphilic $(DPS\text{-}b\text{-}PGA)_n$ films is challenging, due to the different affinities of the hydrophobic PS and hydrophilic PGA blocks. However, by doing thermal annealing above their glass transition temperatures, the polymer chains can easily rearrange into a thermodynamically

stable configuration, offering a more practical and effective alternative. AFM measurements show that the linear BCP (N_{BB} = 1) had a morphology at the surface with parallel lamellae, as evidenced by the island and holes in the height image, and vertical lamellae, as evidenced by the fingerprint patterns at the edges of the island and holes (**Figure 2a**, **Figure S6a**). Increasing N_{BB} to 5, 25, 50 and 100 resulted in a larger fraction of normal oriented lamellae to the surface (**Figure 2b-2d, Figure S6-S7**). Interference microscopy (**Figure S8**) at the edge of the BBCP thin film was performed to investigate the lamellae orientation.[33] The linear BCP shows discrete changes in the interference colors, indicative of an orientation of the lamellar microdomains parallel to the substrate interface that propagated through the film. In contrast, increasing N_{BB} to 5, 25, 50 and 100 showed only small changes in the interference colors, indicating a reduced parallel orientation within the thin film. The 2D GISAXS profiles above the critical angle of the polymer ($\alpha_{cp} = 0.18°$)[8, 34, 35] showed that the linear BCPs had a mixture of lamellae oriented both parallel and normal to the surface, while the polymer with higher N_{BB} produced exclusively lamellae oriented normal to the surface (**Figure S9**), consistent with AFM and interference microscopy data. 1D linecuts of GISAXS profiles in the in-plane direction showed interference maxima corresponding to d-spacings of 17.5, 18.2, 18.4, 18.5, and 18.8 nm for N_{BB}=1, 5, 25, 50, and 100, respectively (**Figure S10**).

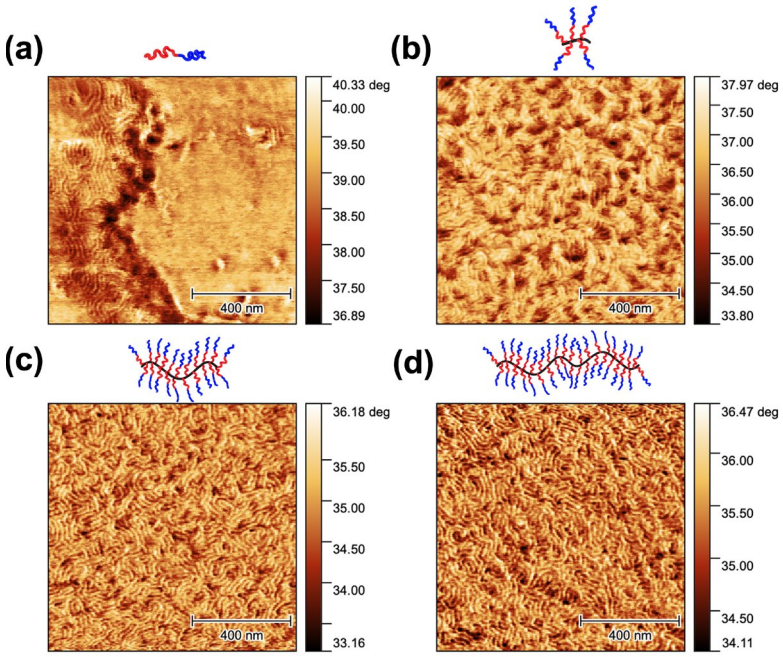

Figure 2. AFM phase images of BBCP thin films with different N_{BB} values. (a) $N_{BB} = 1$ (linear). (b) $N_{BB} = 5$ (star-like). (c) $N_{BB} = 50$ (rod-like). (d) $N_{BB} = 100$ (worm-like).

In previous studies, we showed that GISANS is more sensitive than GISAXS for characterizing the depth dependence of polymer morphology in thin films. GISANS also enables a selective investigation of near-substrate morphologies by passing the incident beam through the substrate (i.e., negative incidence angles).[8] By calculating the scattering depth of X-rays and neutrons in the BBCP thin film yields the depth from which scattering is detected,[8, 36] with the scattering depth, *D*, given by

$$D = \frac{\lambda}{\sqrt{2}\pi(l_i + l_f)} \tag{1}$$

$$l_{i,f} = [(\alpha_c^2 - \alpha_{i,f}^2) + \sqrt{\alpha_c^2 - \alpha_{i,f}^2 + 4\beta^2}]^{\frac{1}{2}} \tag{2}$$

Here, D represents the depth from which a scattering event can be detected with a characteristic intensity decay length of 1/e of the radiation incident on the surface at an angle α_i and exiting the sample at angle α_f, λ is the wavelength of the incident radiation, α_c is critical angle at the polymer-air or polymer-substrate interface. For X-rays, β is imaginary part of the effective refractive index due to the attenuation of the radiation as it enters and is scattered by the sample. For X-rays, this arises from the absorption due to the chemical composition of the sample, while for neutrons the attenuation arises primarily from the incoherent scattering. Both are calculable and measurable quantities.[37, 38] As shown in **Figure S11**, the scattering depth of GISAXS increases by several orders of magnitude when the X-ray incidence angle exceeds the critical angle of the polymer-air surface, due to negligible X-ray absorption However, the significant incoherent scattering of neutrons by the hydrogenated polymers leads to a gradual transition of scattering depth at higher neutron incidence angles, from a few nanometers to tens of nanometers.

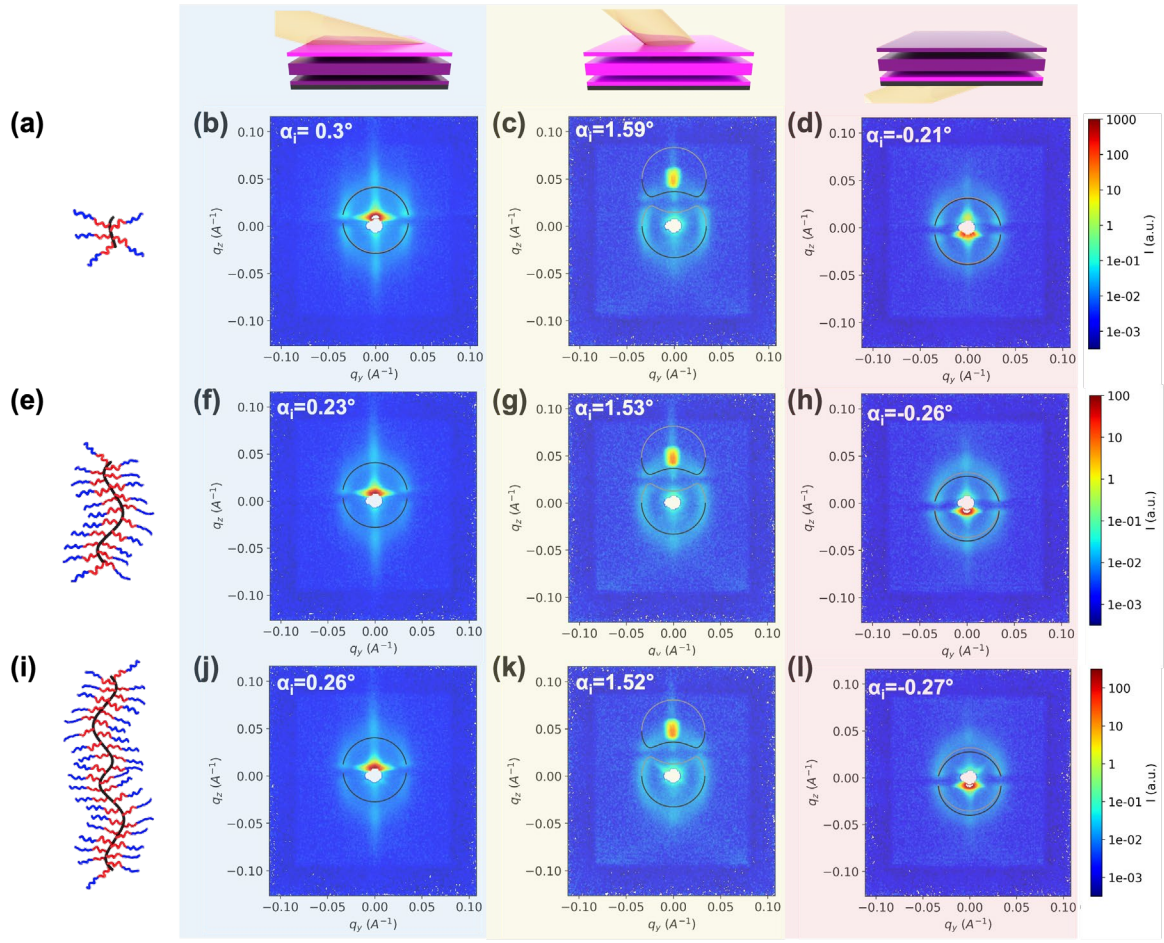

Figure 3. Depth dependent morphology of BBCP thin film with varying N_{BB} as measured by GISANS. N_{BB}=5: (a) Scheme; (b) Near-air surface (α_i = 0.3°); (c) Bulk of thin film (α_i = 1.59°); (d) Near-substrate surface (α_i = -0.21°). N_{BB}=50: (e) Scheme; (f) Near-air surface (α_i = 0.23°); (g) Bulk of thin film (α_i = 1.53°); (h) Near-substrate surface (α_i = -0.26°). N_{BB}=100: (i) Scheme; (j) Near-air surface (α_i = 0.26°); (k) Bulk of thin film (α_i = 1.52°); (l) Near-substrate surface (α_i = -0.27°). The incidence angle was calculated precisely from the specular reflection. The grey and black lines represent the upper and lower rings predicted by the Debye-Scherrer equation based on the in-plane peak fitting from equations (3)-(6). When the incident angle is close to the critical incident angle, the upper and lower rings merge.

GISANS experiments were then performed on the linear BCP (N_{BB} = 1) at incidence angles of 0.36°, 1.59°, 3.04°, -0.27°, and -0.88° to systematically investigate thin film morphologies at different depths (**Figure S12**). The critical angle for polymer-air (α_{cp}) and polymer-substrate (α_{cs}) interfaces were calculated as 0.39° and -0.33°, respectively, indicating that the selected incidence angles effectively probed the morphologies near the air surface, in the bulk of thin film, and near the substrate interface. In the 2D GISANS patterns, strong out-of-plane peaks and weak in-plane peaks were observed at α_i = 0.39° and at α_i = -0.27°, respectively, indicating a predominant (though not exclusive) orientation of the lamellar microdomains parallel to the substrate. With increasing incidence angle (i.e., deeper penetration), the out-of-plane peaks persisted but with reduced relative intensities, while the in-plane peaks broadened azimuthally at incidence angles of 1.59°, 3.04°, -0.88°. As shown in **Figures 3c**, **3g**, and **3k**, the relative intensity of the in-plane peak is significantly stronger in Debye–Scherrer ring pattern for N_{BB} = 5. As the backbone length increases to N_{BB} = 50 and 100, the peak intensity differences along the Debye–Scherrer (DS) ring diminish, indicating a transition from a vertical alignment toward a more random orientation at higher N_{BB} values. These results are consistent with previous reports for PS-*b*-PGM linear BCP thin film.[8]

Using an incidence angle close to the critical angle of the polymer, the 2D GISANS will show Debye-Scherrer (DS) rings at scattering vectors as given by[8, 39-42]

$$q_z = k_{iz} + (k_{cP}^2 + \{[(2\pi m/L_0)^2 - q_y^2)^{\frac{1}{2}} \pm (k_{iz}^2 - k_{cP}^2)^{1\frac{1}{2}}\}^2)^{\frac{1}{2}} \quad (3)$$

$$q_z = k_{iz} - (k_{cSP}^2 + \{[(2\pi m/L_0)^2 - q_y^2)^{\frac{1}{2}} \pm (k_{iz}^2 - k_{cP}^2)^{\frac{1}{2}}\}^2)^{\frac{1}{2}} \quad (4)$$

$$q_z = k_{iz} + (k_{cP}^2 + \{[(2\pi m/L_0)^2 - q_y^2)^{\frac{1}{2}} \pm (k_{iz}^2 - k_{cSP}^2)^{\frac{1}{2}}\}^2)^{\frac{1}{2}} \quad (5)$$

$$q_z = k_{iz} - (k_{cSP}^2 + \{[(2\pi m/L_0)^2 - q_y^2)^{\frac{1}{2}} \pm (k_{iz}^2 - k_{cSP}^2)^{\frac{1}{2}}\}^2)^{\frac{1}{2}} \quad (6)$$

where q_z and q_y represent the scattering vector z and y components, respectively. k_{iz}, k_{cP} and k_{cSP} denote wavevectors of the incidence neutrons and the critical wave vectors at the polymer-air and polymer-substrate interfaces, respectively. L_0 is the center-to-center distance between adjacent microdomains, and m is the scattering order (m = 1 is used). We note that equations (3)-(4) and (5)-(6) were used when neutrons entered from the air and substrate interfaces, respectively.

It is also important to note that with GISANS, using the Distorted-Wave Born Approximation (DWBA), the intensity is significantly influenced by multiple scattering and wave interference effects. At grazing incidence, the neutron wave is distorted by reflection and refraction at the film–air and film–substrate interfaces, and the observed scattering pattern results from interference between various transmission and reflection channels. Consequently, the azimuthal angle in GISANS does not map cleanly to the real-space orientation of scattering domains. For this reason, plotting intensity vs. azimuthal angle in GISANS does not provide a direct or reliable measure of the degree of orientation, as in the transmission geometry, which has been discussed in the literature.[43-47]

As shown in **Figure 3b**, **3f** and **3j**, for N_{BB} = 5 (star-like) the scattering was dominated by in-plane peaks, while N_{BB} = 25(rod-like) and 100 (worm-like) produced more random orientations, as evidenced by the reduced intensity for the in-plane peaks. The 2D GISANS patterns were fit based on the in-plane peaks, where for all configurations the out-of-plane peak q values were higher than predicted by the DS ring, indicating a smaller domain spacing in the out-of-plane direction. The summarized 1D line cut of the 2D GISANS patterns for different N_{BB} in the in-plane direction (**Figure 4a**) show star-like BBCPs to have the strongest in-plane peak intensities, while linear BCPs had the weakest. The out-of-plane direction showed the opposite behavior (**Figure 4b**). At higher incidence angles ($\alpha_i \approx 1.59°$) where the bulk of film is probed, the out-of-plane peaks

persisted for all configurations, but the in-plane peaks became azimuthally broader for higher N_{BB}. Similar 2D GISANS patterns were observed at higher incidence angles, e.g., $\alpha_i \approx 0.85°$ and $\alpha_i \approx -0.87°$ (**Figure S13**). Consequently, the relative peak intensity in both in-plane and out-of-plane directions for the bulk (**Figure 4c, 4d** and **Figure S14**) show a more random orientation. It was not possible to perform an polar transformation of the GISANS patterns, due to limitations imposed by distorted Born approximation in the GI geometry, precluding a determination of the preferred BBCP orientation. At small negative incidence angles ($\alpha_i \approx -0.29°$), which selectively probe near the substrate interface, the 2D GISANS patterns (**Figure 3d, 3h** and **3i**) and integrated intensities (**Figure 4e** and **Figure 4f**) suggest star-like BBCP to have the strongest in-plane lamellar orientation and the weakest out-of-plane lamellar orientation among all configurations. Higher N_{BB}s, including rod-like and worm-like linear BBCPs, had more random orientations, consistent with the GISANS results near the air surface. Additionally, the near-substrate interface appeared to have a relatively higher peak intensity compared to the near-air interface. However, the observed intensities also included background scattering, where the background contribution may vary at different incidence angles, making direct comparison between different incidence angles potentially misleading. In summary, increasing N_{BB} from 1 (linear) to 5 (star-like) promotes a vertical lamellar orientation, as the entropic penalty associated with a parallel orientation becomes too high. If star-like BBCPs assume a parallel orientation, all side chains must orient in the same direction (towards substrate) to maximize surface interactions between the PGA block and the substrate. This can impose significant conformational constraints, especially near the backbone. When the entropic penalty associated with parallel orientation outweighs the enthalpic loss by unfavorable contacts between the PS block and the substrate, the star-like BBCP would form vertical lamellae by orienting the arms parallel to the substrate with side chains orienting in

the opposite direction (**Scheme 2**). Increasing N_{BB} further, into the rod- and worm-like regimes, makes a uniform side chain orientation energetically unfavorable due to overcrowding. Instead, side chains must extend from the backbone, orienting in different directions, leading to a random orientation at higher N_{BB}. In general, the orientation becomes more random within the bulk of thin film, as the influence of surface interactions diminishes, in keeping with previous studies on linear PS-*b*-PSM.[6-9]

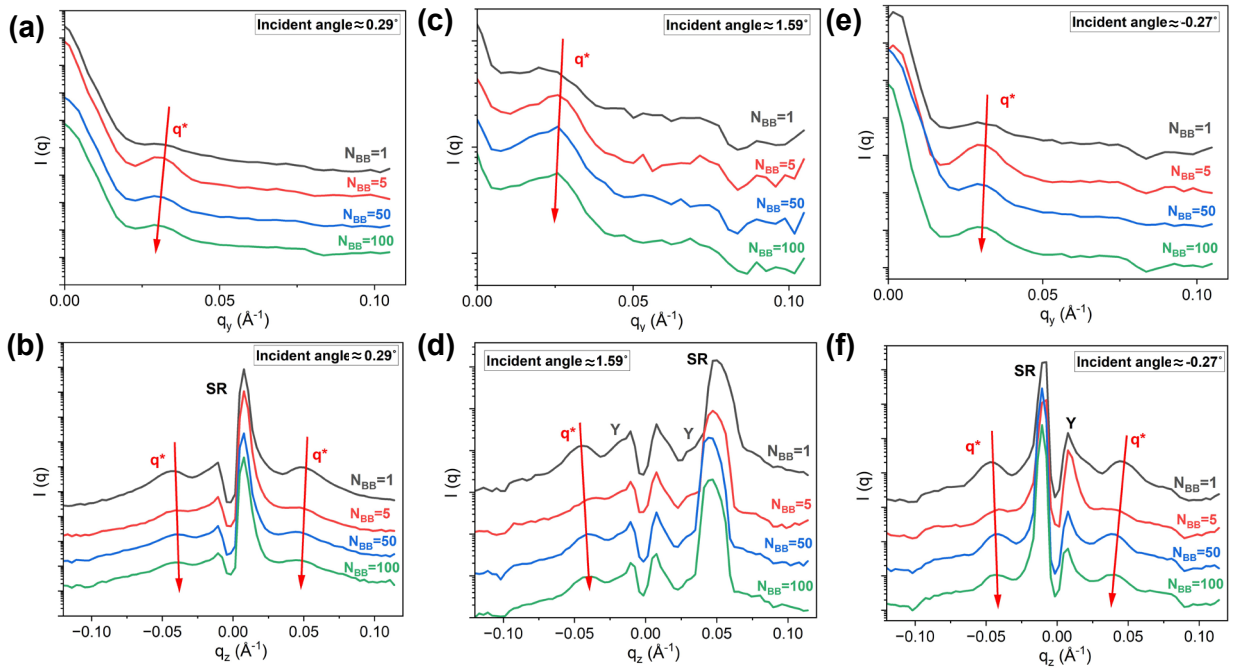

Figure 4. 1D linecut integral of 2D GISANS images for probing depth-dependent morphology of thin films. Near-air surface: (a) In-plane direction at $q_z = 0$; (b) Out-of-plane direction at $q_y = 0$. In the bulk of thin film: (c) In-plane direction at $q_z = 0$; (d) Out-of-plane direction at $q_y = 0$. Near-substrate surface: (e) In-plane direction at $q_z = 0$; (f) Out-of-plane direction at $q_y = 0$. Arrows indicate the trend of primary peak with increasing N_{BB}. The Y, and SR denote the Yoneda peak and specular reflection, respectively.

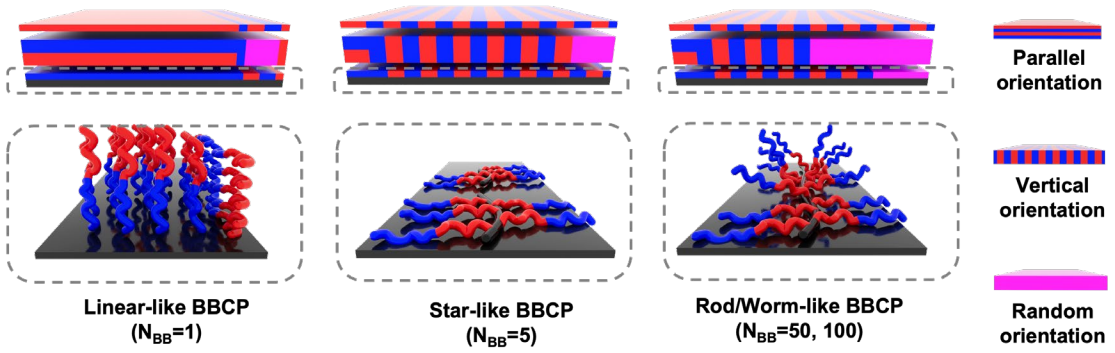

Scheme 2. Schematic illustration of depth-dependent morphology with varying N_{BB}. The dash box indicates the potential BBCP conformation near the substrate surface.

Effect of grafting density on the BBCP thin film morphology

The restricted flexibility of side chains imposed by higher N_{BB} in the bottlebrush architecture can be alleviated by reducing the GD. For example, GD was varied for N_{BB} = 50 from 100% to 75% to 50%. AFM phase images (**Figure 5a-5c**) showed that BBCPs of all three GDs produced a uniform orientation of the lamellar microdomains normal to the air surface. This is consistent with interference microscopy measurements **(Figure S16**) where only gradual changes in the interference colors were evident for all three GDs. Further corroboration came from GISAXS measurements (**Figure S17**) that showed only in-plane reflections. We used GISANS to investigate depth-dependent morphologies by varying the incidence angle. At small incidence angles (α_i!≈ 0.29°) for probing near the air surface, GISANS patterns showed predominantly in-plane peaks, with the degree of orientation increasing at lower GD, as shown in **Figure S18**. At higher incidence angles, the in-plane peaks broadened azimuthally, whereas the relative intensity of the in-plane peak increased, and out-of-plane peaks became weaker as GD decreased. At a small negative incidence angle (α_i!≈ -0.27°) that selectively probes the substrate interface, the relative in-plane

peak intensity increased with lower GD, with minimal changes in the out-of-plane peaks (**Figure 5d-5f**). As summarized in **Figure 5g**, a lower GD of rod-like BBCP enhances side-chain flexibility, where the entropic penalty associated with a parallel orientation remains high, even with a reduced number of side chains per molecule. However, the entropic penalty for aligning all side chains in a uniform direction significantly decreases. Consequently, lower GD values in high N_{BB} BBCPs promote an orientation normal to the substrate, although random orientation persists within the bulk of thin film.

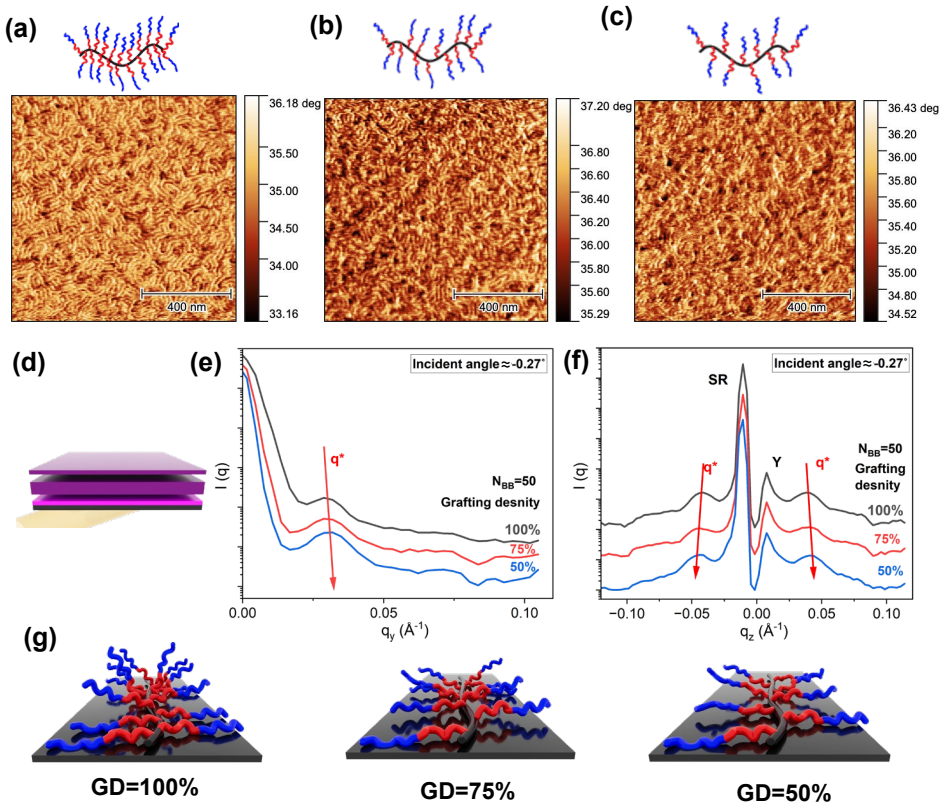

Figure 5. Effect of GD on depth-dependent morphology of BBCP thin film (N_{BB} = 50). AFM phase images of (a) GD = 100%, (b) GD = 75% and (c) GD = 50%. 1D linecut integral of 2D GISANS images for probing near-substrate surface (α_i!≈ -0.27°): (d) Schematic illustration; (e) In-plane direction; (f) Out-of-plane direction. (g) Hypothesized BBCP conformation near substrate surface.

Effect of backbone confinement on the BBCP thin film morphology

The experiments described to this point used a silicon substrate, where the hydrophilic corona block (PGA block) prefers the polar substrate, and the hydrophobic core block (PS block) avoids direct contact, if only enthalpic interaction is considered. However, in the equilibrated morphology, the hydrophobic core is forced to contact the substrate, due to the entropic penalty dominating the free energy where the attachment of the core blocks to the backbone limits the chain flexibility. Previous studies on star BCPs at homopolymer interfaces showed that the corona block, when positioned further from the central junction, had greater flexibility than the core block, assuming orientations similar to that seen with linear BCPs.[28] To better understand the effect of backbone confinement on BBCP thin film morphology, we modified the substrate by anchoring hydroxyl-terminated PS to the surface.[48] The successful anchoring of a thin layer of PS onto silicon substrate was confirmed by water contact angle (WCA) and X-ray reflectivity (**Figure S19**) measurements. This modification switches the preferential interactions of BBCP with the substrate from the corona to core block. AFM phase images showed that for $N_{BB} = 5$, the thin film showed a uniform surface (**Figure 6b**). However, as N_{BB} increased to 50, fingerprint patterns began to appear randomly across the surface (**Figure 6g**). At $N_{BB} = 100$, the areal density of fingerprints increased (**Figure 6i**). Interference microscopy (**Figure S22**) showed sharp, well-defined changes in the interference colors only for $N_{BB} = 5$, in agreement with AFM data. To investigate the depth-dependent morphology, GISANS experiments at various angles of incidence were performed. BBCPs with $N_{BB} = 5$ showed predominantly out-of-plane peaks near the air surface, in the interior of the thin film, and near the substrate interface (**Figure 6c-6e**). For BBCPs with $N_{BB} = 50$ and 100, a random orientation was found at all depths of the thin film (**Figure 6h-6j**, **6m-6o** and **Figure**

S23). The 1D linecut integral of 2D GISANS images (**Figure 7**) showed predominantly in-plane peaks on a hydrophilic substrate but predominantly out-of-plane peaks on a hydrophobic substrate at both the air and the substrate interfaces when $N_{BB} = 5$. As N_{BB} increased to 50 and 100, the in-plane peaks weakened while the out-of-plane peaks strengthened on the hydrophilic substrate, at both interfaces. This was reversed on hydrophobic substrates, and the orientation arising from the substrate interactions also propagates to the air interface. The GISANS data arising from both hydrophobic and hydrophilic substrates are due to a greater loss of orientation for higher N_{BB}. As summarized in **Scheme 3**, when the interactions between the core block and the substrate are maximized, the corona block of star-like BBCPs can avoid direct contact with the substrate without a significant entropic penalty, giving rise to an orientation of the lamellae parallel to the substrate. As N_{BB} increases, the BBCPs adopt rod-like and worm-like shapes, and the side chains must extend from the backbone to prevent overcrowding. This leads to a more random orientation at higher N_{BB}, independent of substrate modification.

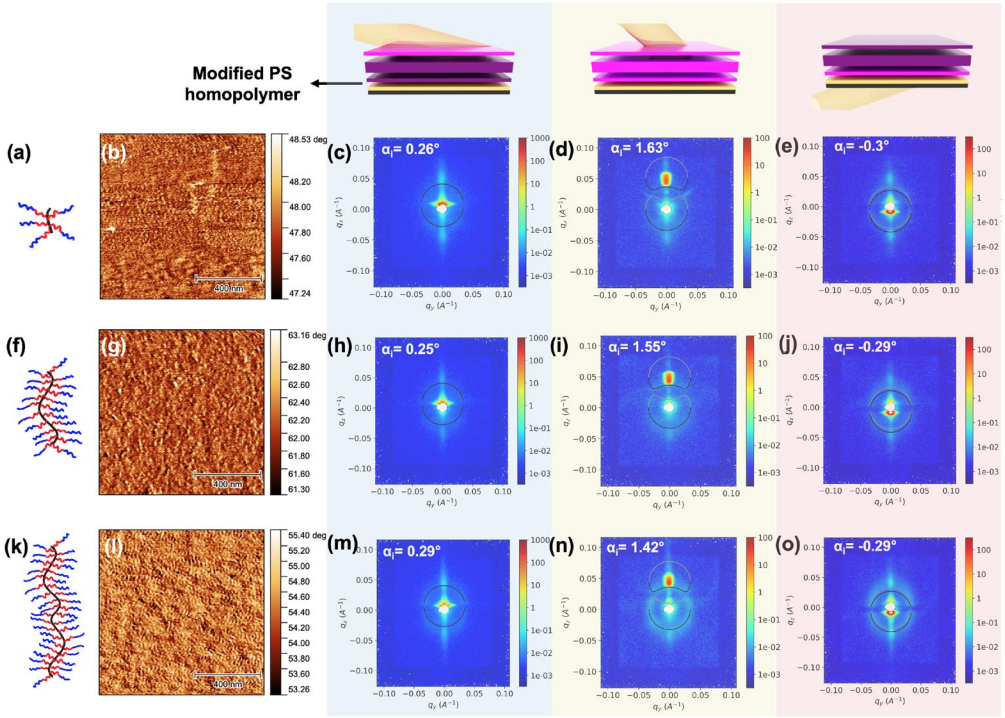

Figure 6. Effect of backbone confinement on BBCP thin film morphology by modification of substrate with PS homopolymer, as function of N_{BB}. N_{BB} = 5: (a) Scheme; (b) AFM phase images. (c) Near-air surface (α_i = 0.26°); (d) Bulk of thin film (α_i = 1.63°); (e) Near-substrate surface (α_i = -0.3°). N_{BB} = 50: (a) Scheme; (b) AFM phase images. (c) Near-air surface (α_i = 0.25°); (d) Bulk of thin film (α_i = 1.55°); (e) Near-substrate surface (α_i = -0.29°). N_{BB} = 100: (a) Scheme; (b) AFM phase images. (c) Near-air surface (α_i = 0.29°); (d) Bulk of thin film (α_i = 1.42°); (e) Near-substrate surface (α_i = -0.29°). The incidence angle was calculated precisely from the specular reflection. The grey and black lines represent the upper and lower rings predicted by the Debye-Scherrer equation based on the in-plane peak fitting from equation (3)-(6). When the incident angle is close to the critical incident angle, the upper and lower rings merge.

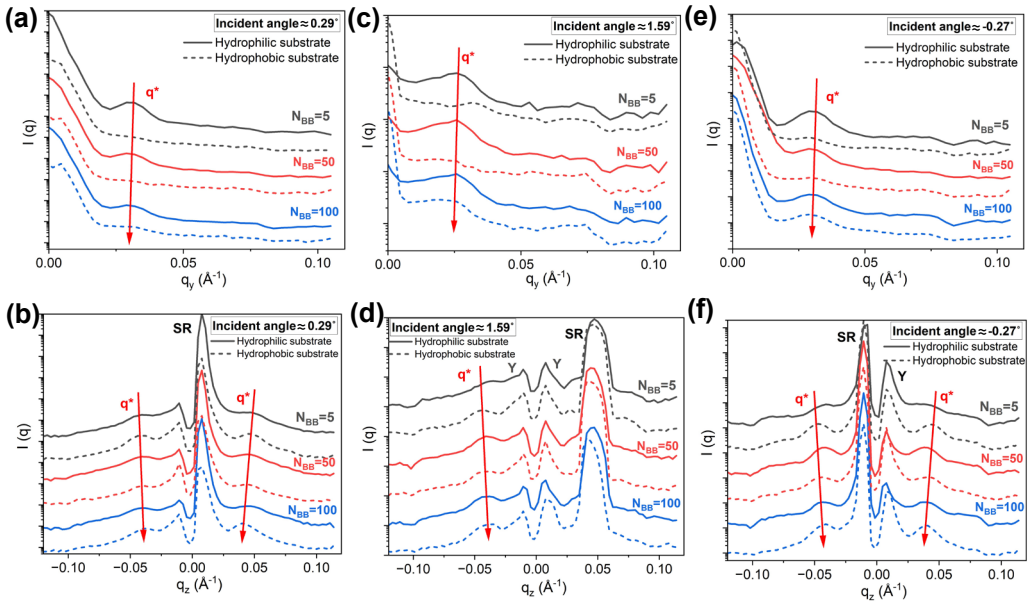

Figure 7. 1D linecut integral of 2D GISANS images for probing depth-dependent morphology of thin film with and without substrate modification as a function of N_{BB}. Near-air surface: (a) In-plane direction at q_z = 0; (b) Out-of-plane direction at q_y = 0. In the bulk of thin film: (c) In-plane direction at q_z = 0; (d) Out-of-plane direction at q_y = 0. Near-substrate surface: (e) In-plane direction

at q_z = 0; (f) Out-of-plane direction at q_y = 0. Arrows indicate primary peak changes on the hydrophobic substrate. The Y and SR denote the Yoneda peak and specular reflection, respectively.

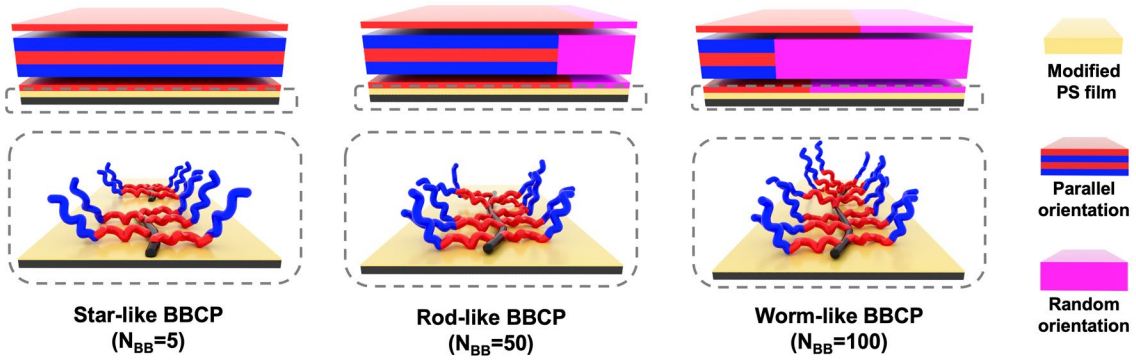

Scheme 3. Schematic illustration of depth-dependent morphology for PS homopolymer modified substrate as function of N_{BB}. The dash box indicates the potential BBCP conformation near the substrate surface.

We also investigated the effect of GD on the BBCP morphology on hydrophobic substrates. At a 50% GD, AFM phase images showed a larger fraction of the surface covered with fingerprint patterns, i.e., lamellae oriented normal to the surface, in comparison to 100% GD (**Figure 8a** and **8b**). This result is consistent with GISANS data that show a higher in-plane peak intensity for 50% GD (**Figure 8c**). On a hydrophobic substrate, **Figure 8d** indicates that the 50% GD sample showed a stronger out-of-plane peak in comparison to BBCPs with 100% GD. Similarly, 50% GD also showed relatively stronger in-plane and out-of-plane peaks near the substrate surface (**Figure 8g** and **8h**). These results indicate that a lower GD facilitates a more ordered orientation, whether parallel or perpendicular, at both the air and the substrate interfaces. It was also seen that the DS

ring intensity was enhanced for lower GD at different depths (**Figure S24**), which may be associated with a higher SLD difference between domains due to a collapsed conformation of side chains. In summary, compared to a hydrophilic substrate, hydrophobic substrates result in significantly weakened in-plane peaks with predominantly out-of-plane peaks at different depths, consistent with the effects observed when varying N_{BB}.

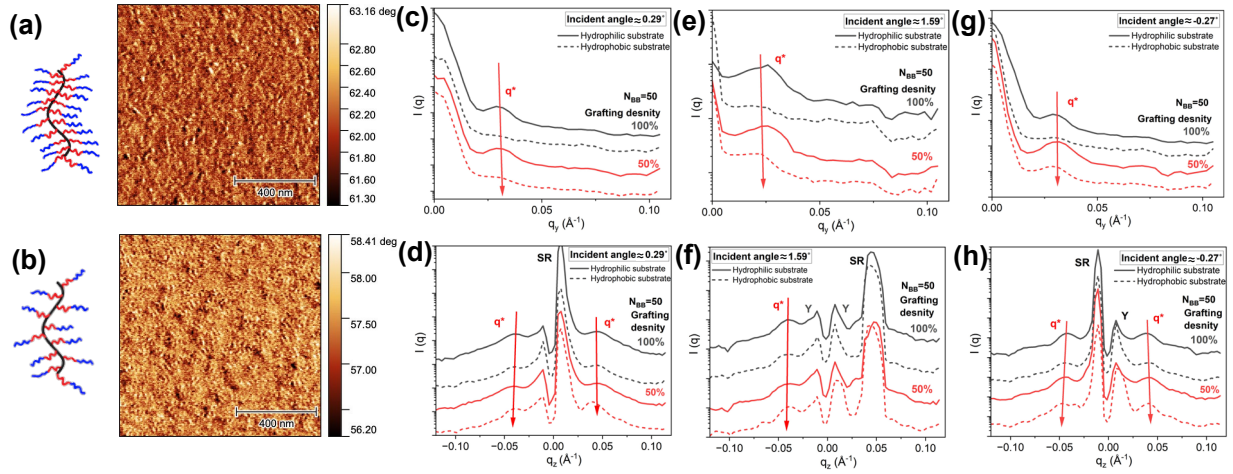

Figure 8. Effect of GD on BBCP thin film (N_{BB} = 50) morphology with and without substrate modification. GD = 100%: (a) Schemes (b) AFM phase images on modified substrate. GD = 50%: (c) Schemes (d) AFM phase images on modified substrate. 1D linecut integral of 2D GISANS images for probing depth-dependent morphology: Near-air surface for (e) in-plane direction at q_z = 0 and (f) out-of-plane direction at q_y = 0; In the bulk of thin film for (g) in-plane direction at q_z = 0 and (h) out-of-plane direction at q_y = 0; near-substrate interface for (i) in-plane direction at q_z = 0 and (j) out-of-plane direction at q_y = 0. Arrows indicate primary peak changes on hydrophobic substrate. The Y and SR denote the Yoneda peak and specular reflection, respectively.

Conclusion

We synthesized a series of bottlebrush block copolymers (BBCPs) consisting of deuterated polystyrene (DPS) as the core block and poly(solketal acrylate) (PSA) as the corona block, with varied backbone lengths (N_{BB}) and grafting densities (GD). Uniform BBCP thin films were prepared by spin-coating onto silicon substrates, followed by TFA-induced hydrolysis to convert hydrophobic PSA into hydrophilic PGA, bringing the BBCP from the disordered state into a strongly microphase-separated state. The resultant depth-dependent morphology was investigated systematically by atomic force microscopy (AFM), interference microscopy, grazing-incidence small angle X-ray scattering (GISAXS) and grazing-incidence small angle neutron scattering (GISANS). The results showed that for $N_{BB} = 1$ (linear), a mixture of parallel and perpendicular lamellae orientations near the air and the substrate interfaces was found. For $N_{BB} = 5$ (star-like BBCP), the lamellar microdomains were oriented predominantly normal to both the air and substrate interfaces. By increasing N_{BB} to 25, 50, and 100, the orientation of the microdomains was lost and a more random orientation was found. This behavior arises from the orientation of the side chains in the same direction to maximize favorable interactions (enthalpy) between the PGA block and the substrate while avoiding contact of the substrate with the PS block imposing a significant entropic penalty. For higher N_{BB} (rod-like and worm-like configurations), side chain packing results in overcrowding, and the side chains splay from the backbone, giving rise to a more randomized orientation. This steric hindrance effect can be alleviated by reducing GD by the incorporation of spacer groups into the backbone, where lower GDs (75% and 50%) facilitated a more uniform orientation of the microdomains normal to the surface. In general, the orientation dissipates with increasing distance from the interfaces. By anchoring a PS layer to the substrate, preferential interactions of the BBCP with substrate shift from the corona to core block. Under these conditions, the star-like BBCP ($N_{BB} = 5$) showed predominantly parallel microdomain

orientation. With a hydrophilic substrate, the core block preferentially interacts with the substrate. Higher N_{BB} copolymers showed a more randomized orientation at different depths in thin films. Overall, this work demonstrates the strategic use of entropic effects to control the BCP thin film morphology, with the entropy contribution precisely tuned through BBCP architectural design, including variations in N_{BB}, GD, and backbone constraints.

Acknowledgement

This work was supported by Air Force Office of Scientific Research under contract number FA9550-25-1-0003 with project number 24RT0450 and the Army Research Office under Contract No. W911NF-24-2-0041. A portion of this research used resources at the Spallation Neutron Source, a DOE Office of Science User Facility operated by the Oak Ridge National Laboratory. The beam time was allocated to EQ-SANS on proposal number IPTS-30441.

Author Contributions

The manuscript was written with contributions from all authors. All authors approve the final version of the manuscript.

Materials and Methods

Materials. Toluene and trifluoroacetic acid (TFA) were purchased from Sigma-Aldrich. Deuterated styrene-d8 and Ω-hydroxyl terminated polystyrene (PS-OH, Mn: 6000 g/mol) were

purchased from Polymer Source Inc. Details of other synthesis materials can be found in the **Supporting Information**. Silicon wafers were purchased from International Wafer Service, Inc. (IWS) and cleaned with previously developed methods prior to use.[28] After cleaning, the Si wafers have a hydrophilic surface due to the natural SiO_2 layer on top. To prepare hydrophobic Si wafer, PS-OH solution was spin-coated onto the substrate and then thermal annealed at 160 °C under vacuum overnight, followed by soaking in toluene solution for a few hours to remove unreacted PS-OH polymer.

Synthesis of Bottlebrush Block Copolymers. Bottlebrush block polymers (BBCPs) were synthesized from linear diblock macromonomers (MMs), specifically comprised of poly(solketal acrylate) (PSA) blocks and deuterated polystyrene (DPS) with polymerizable norbornene groups covalently tethered. The MMs DPS-PSA (M_n = 11.6 kDa, f_{DPS} = 0.31) was prepared via atom transfer radical polymerization (ATRP) and consistently employed throughout the research. Utilizing the Grubbs 3rd catalyst (G3, $(H_2IMes)(Cl)_2(pyr)_2RuCHPh$), the bottlebrush BCP polymers were obtained by ROMP of the MMs. This process yielded a bottlebrush polymer with DPS as the core and PSA as the corona. The backbone length (N_{BB}) was modulated by adjusting the feed ratio of MMs to G3, ranging from 5, 25, 50 to 100. Furthermore, the graft density (GD) of bottlebrush BCPs was controlled by copolymerizing MMs with a phenyl-substituted norbornene (NB-Ph) monomer. At a fixed total N_{BB}, GD was regulated by the ratio between NB-Ph and DPS-PSA macromonomer. Detailed information regarding the synthesis and their characterizations can be found in the **Supporting Information**.

Solid State Conversion of Bottlebrush BCP Thin Film with TFA Vapor. Bottlebrush BCPs were dissolved in toluene solution at 12 mg/ml and spin-coated onto the top of the silicon substrate at a spin speed of 2000 rpm for 60 s to produce ~50 nm thick films. To convert hydrophobic PSA

block to hydrophilic PGA block, the polymer films were then exposed to TFA vapor (TFA to water volume ratio 3:1) in a sealed glass jar for 3 h to complete the reaction. After that, the films were removed from the jar, followed by thermal annealing to obtain equilibrium morphology at 150 °C for 24 h. The detailed studies were previously published.

Atomic Force Microscopy (AFM). AFM was employed to characterize the air-surface morphology of bottlebrush BCP thin film. It was performed on an Asylum MFP-3D under tapping mode. The AFM probes were purchased from Bruker with model NCHV.

Interference Microscopy. Interference microscopy was performed on OLYMPUS BX60 with U-MDIC differential interference contrast cube inserted for investigating the edge of polymer thin films.

Small-Angle X-ray Scattering (SAXS). The morphology and d-spacing of bottlebrush BCP in bulk were characterized by SAXS. The DPS-PSA bottlebrush sample powder was compression into sample washer, followed by solid-state conversion and thermal annealing under the same conditions as thin film samples. SAXS experiments were conducted on Ganesha SAXS-lab instrument (Cu $K\alpha$ radiation, λ = 0.1542 nm), with a Pilatus 300K 2D detector.

Grazing-Incidence Small-Angle X-ray Scattering (GISAXS). GISAXS experiments were performed on Ganesha SAXS-lab instrument (Cu $K\alpha$ radiation, λ = 0.1542 nm) with a Pilatus 300K 2D detector. All measurements were performed in vacuum at an incidence angle of 0.18° (above the critical incidence angle of polymer-air surface) to characterize the whole thin film morphology. The red and pink lines in 2D GISAXS images are the upper and lower rings predicted by Debye-Scherrer equations based on in-plane peaks using Python package developed by previous publications (https://github.com/mingqiuhu/XRayScatterPy).[49]

X-ray Reflectivity (XRR). X-ray reflectivity was conducted on Ganesha SAXS-lab instrument (Cu $K\alpha$ radiation, λ = 0.1542 nm) equipped with a Pilatus 300K 2D detector. A series of specular reflections were obtained at various incidence angle of X-ray beam. The specular reflection intensities were extracted from the corresponding 2D detector images and plotted as a function of scattering vector (q) using a previously developed Python package (https://github.com/mingqiuhu/XRayScatterPy).[49]

Grazing-Incidence Small-Angle Neutron Scattering (GISANS). To analyze depth-dependent morphology of bottlebrush BCP thin film, GISANS was performed with the EQ-SANS instrument of Spallation Neutron Source at Oak Ridge National Lab.[50] Given that the neutron wavelength at 7 Å has the highest abundance, the neutron wavelength is taken as 7 Å for the calculation of the momentum transfer, q, using equation $q = 4\pi\sin(\alpha_i)/\lambda$, where α_i is incidence angle and λ is neutron wavelength. The incidence angle of bottlebrush thin film was controlled by rotation of a goniometer, with the precise incidence angle determined from the specular reflection observed from 2D GISANS images. Data reduction into 2D followed standard procedures that are implemented in the drtsans data reduction software.[51] The grey and black lines above $q_z = 0$ correspond to the lower and upper rings predicted by the Debye-Scherrer equations where neutrons exit on top of thin film, while the grey and black line below $q_z = 0$ are the lower and upper rings predicted by Debye-Scherrer equations where neutron exits below the silicon substrate. The fitting of data was based on the in-plane peaks in the GISANS images.

References

(1) Hawker, C. J.; Russell, T. P. Block Copolymer Lithography: Merging "Bottom-Up" with "Top-Down" Processes. *MRS Bulletin* **2011**, *30* (12), 952-966. DOI: 10.1557/mrs2005.249.
(2) Bates, C. M.; Maher, M. J.; Janes, D. W.; Ellison, C. J.; Willson, C. G. Block Copolymer Lithography. *Macromolecules* **2013**, *47* (1), 2-12. DOI: 10.1021/ma401762n.

(3) Sinturel, C.; Bates, F. S.; Hillmyer, M. A. High chi-Low N Block Polymers: How Far Can We Go? *ACS Macro Lett* **2015**, *4* (9), 1044-1050. DOI: 10.1021/acsmacrolett.5b00472 From NLM PubMed-not-MEDLINE.
(4) Bates, F. S.; Fredrickson, G. H. Block copolymer thermodynamics: theory and experiment. *Annu Rev Phys Chem* **1990**, *41*, 525-557. DOI: 10.1146/annurev.pc.41.100190.002521 From NLM PubMed-not-MEDLINE.
(5) Jeong, G.; Yu, D. M.; Mapas, J. K. D.; Sun, Z.; Rzayev, J.; Russell, T. P. Realizing 5.4 nm Full Pitch Lamellar Microdomains by a Solid-State Transformation. *Macromolecules* **2017**, *50* (18), 7148-7154. DOI: 10.1021/acs.macromol.7b01443.
(6) Yu, D. M.; Smith, D. M.; Kim, H.; Mapas, J. K. D.; Rzayev, J.; Russell, T. P. Morphological Evolution of Poly(solketal methacrylate)-block-polystyrene Copolymers in Thin Films. *Macromolecules* **2019**, *52* (10), 3592-3600. DOI: 10.1021/acs.macromol.9b00488.
(7) Hu, M.; Li, X.; Rzayev, J.; Russell, T. P. Hydrolysis-Induced Self-Assembly of High-χ–Low-N Bottlebrush Copolymers. *Macromolecules* **2021**, *54* (24), 11449-11458. DOI: 10.1021/acs.macromol.1c02061.
(8) Hu, M. Q.; Li, X. D.; Heller, W. T.; Bras, W.; Rzayev, J.; Russell, T. P. Using Grazing-Incidence Small-Angle Neutron Scattering to Study the Orientation of Block Copolymer Morphologies in Thin Films. *Macromolecules* **2023**, *56* (6), 2418-2428. DOI: 10.1021/acs.macromol.2c02415.
(9) Hu, M.; Li, X.; Rzayev, J.; Russell, T. P. Hydrolysis-Induced Morphology Evolution of Linear and Bottlebrush Block Copolymers in Thin Films with Acid Vapor or Photoacid Generators. *Macromolecules* **2024**, *57* (3), 1128-1137. DOI: 10.1021/acs.macromol.3c02520.
(10) Yu, D. M.; Smith, D. M.; Kim, H.; Rzayev, J.; Russell, T. P. Two-Step Chemical Transformation of Polystyrene-block-poly(solketal acrylate) Copolymers for Increasing χ. *Macromolecules* **2019**, *52* (17), 6458-6466. DOI: 10.1021/acs.macromol.9b01323.
(11) Yu, D. M.; Mapas, J. K. D.; Kim, H.; Choi, J.; Ribbe, A. E.; Rzayev, J.; Russell, T. P. Evaluation of the Interaction Parameter for Poly(solketal methacrylate)-block-polystyrene Copolymers. *Macromolecules* **2018**, *51* (3), 1031-1040. DOI: 10.1021/acs.macromol.7b02221.
(12) Chen, Z.; Hu, M.; Li, X.; Smith, D. M.; Seong, H. G.; Emrick, T.; Rzayev, J.; Russell, T. P. In Situ Hydrolysis of Block Copolymers at the Water-Oil Interface. *Angew Chem Int Ed Engl* **2022**, *61* (25), e202201392. DOI: 10.1002/anie.202201392 From NLM PubMed-not-MEDLINE.
(13) Anastasiadis, S. H.; Russell, T. P.; Satija, S. K.; Majkrzak, C. F. Neutron reflectivity studies of the surface-induced ordering of diblock copolymer films. *Phys Rev Lett* **1989**, *62* (16), 1852-1855. DOI: 10.1103/PhysRevLett.62.1852 From NLM Publisher.
(14) Ryu, D. Y.; Shin, K.; Drockenmuller, E.; Hawker, C. J.; Russell, T. P. A generalized approach to the modification of solid surfaces. *Science* **2005**, *308* (5719), 236-239. DOI: 10.1126/science.1106604 From NLM PubMed-not-MEDLINE.
(15) Kim, S. H.; Misner, M. J.; Xu, T.; Kimura, M.; Russell, T. P. Highly Oriented and Ordered Arrays from Block Copolymers via Solvent Evaporation. *Advanced Materials* **2004**, *16* (3), 226-231. DOI: 10.1002/adma.200304906.
(16) Mansky, P.; Liu, Y.; Huang, E.; Russell, T. P.; Hawker, C. Controlling Polymer-Surface Interactions with Random Copolymer Brushes. *Science* **1997**, *275* (5305), 1458-1460. DOI: 10.1126/science.275.5305.1458.
(17) Walton, D. G.; Kellogg, G. J.; Mayes, A. M.; Lambooy, P.; Russell, T. P. A Free Energy Model for Confined Diblock Copolymers. *Macromolecules* **2002**, *27* (21), 6225-6228. DOI: 10.1021/ma00099a045.

(18) Lo, T.-Y.; Dehghan, A.; Georgopanos, P.; Avgeropoulos, A.; Shi, A.-C.; Ho, R.-M. Orienting Block Copolymer Thin Films via Entropy. *Macromolecules* **2016**, *49* (2), 624-633. DOI: 10.1021/acs.macromol.5b02685.
(19) Lu, K.-Y.; Lo, T.-Y.; Georgopanos, P.; Avgeropoulos, A.; Shi, A.-C.; Ho, R.-M. Orienting Silicon-Containing Block Copolymer Films with Perpendicular Cylinders via Entropy and Surface Plasma Treatment. *Macromolecules* **2017**, *50* (23), 9403-9410. DOI: 10.1021/acs.macromol.7b02218.
(20) Park, S. Y.; Choi, C.; Lee, K. S.; Kim, E.; Ahn, S.; Lee, J.; Kim, J. K. Microdomain Orientation of Star-Shaped Block Copolymer Thin Film Depending on Molecular Weight. *Macromolecules* **2020**, *53* (9), 3611-3618. DOI: 10.1021/acs.macromol.0c00403.
(21) Park, S. Y.; Choi, C.; Jang, J.; Kim, E.; Seo, Y.; Lee, J.; Kim, J. K.; Jeong, H. U.; Kim, J. U. Thin-Film Morphology of Symmetric Six-Arm Star-Shaped Poly(methyl methacrylate)-block-Polystyrene Copolymers. *Macromolecules* **2020**, *54* (1), 316-326. DOI: 10.1021/acs.macromol.0c02384.
(22) Dutta, S.; Wade, M. A.; Walsh, D. J.; Guironnet, D.; Rogers, S. A.; Sing, C. E. Dilute solution structure of bottlebrush polymers. *Soft Matter* **2019**, *15* (14), 2928-2941. DOI: 10.1039/c9sm00033j From NLM PubMed-not-MEDLINE.
(23) Nian, S.; Huang, B.; Freychet, G.; Zhernenkov, M.; Cai, L.-H. Unexpected Folding of Bottlebrush Polymers in Melts. *Macromolecules* **2023**, *56* (6), 2551-2559. DOI: 10.1021/acs.macromol.2c02053.
(24) Chen, Z.; Seong, H. G.; Hu, M.; Gan, X.; Ribbe, A. E.; Ju, J.; Wang, H.; Doucet, M.; Emrick, T.; Russell, T. P. Janus bottlebrush compatibilizers. *Soft Matter* **2024**, *20* (7), 1554-1564. DOI: 10.1039/d3sm01484c From NLM PubMed-not-MEDLINE.
(25) Hu, M.; Seong, H.-G.; Dimitriyev, M. S.; Hu, W.; Chen, Z.; Gan, X.; Grason, G. M.; Emrick, T.; Russell, T. P. Backbone Stitching in Bottlebrush Copolymer Mesodomains and the Impact of Side Chain Crystallization. *Macromolecules* **2025**, *58* (3), 1547-1561. DOI: 10.1021/acs.macromol.4c02589.
(26) Gan, X.; Seong, H.-G.; Hu, M.; Chen, Z.; Emrick, T.; Russell, T. P. Crystallization of Bottlebrush Statistical Copolymers of Polystyrene and Poly(ethylene oxide). *Macromolecules* **2024**, *57* (15), 7306-7314. DOI: 10.1021/acs.macromol.4c01159.
(27) Park, J.; Shin, H.-W.; Bang, J.; Huh, J. Optimizing Chain Topology of Bottle Brush Copolymer for Promoting the Disorder-to-Order Transition. *International Journal of Molecular Sciences* **2022**, *23* (10), 5374.
(28) Chen, Z.; Steinmetz, C.; Hu, M.; Coughlin, E. B.; Wang, H.; Heller, W. T.; Bras, W.; Russell, T. P. Star Block Copolymers at Homopolymer Interfaces: Conformation and Compatibilization. *Macromolecules* **2023**, *56* (20), 8308-8322. DOI: 10.1021/acs.macromol.3c01139.
(29) Gan, X.; Chen, Z.; Steinmetz, C.; Hu, M.; Fink, Z.; Wu, X.; Heller, W. T.; Coughlin, E. B.; Russell, T. P. Architecture-Dependent Thin Film Self-Assembly of Star Polystyrene-poly(2-vinylpyridine) Block Copolymers. *Macromolecules* **2025**, *58* (8), 3832-3840. DOI: 10.1021/acs.macromol.4c03005.
(30) Seong, H. G.; Chen, Z.; Emrick, T.; Russell, T. P. Reconfiguration and Reorganization of Bottlebrush Polymer Surfactants. *Angew Chem Int Ed Engl* **2022**, *61* (19), e202200530. DOI: 10.1002/anie.202200530 From NLM PubMed-not-MEDLINE.
(31) Chen, Z.; Ribbe, A. E.; Steinmetz, C.; Coughlin, E. B.; Hu, M.; Gan, X.; Russell, T. P. Phase Behavior of Charged Star Block Copolymers at Fluids Interface. *Angew Chem Int Ed Engl* **2024**, *63* (11), e202400127. DOI: 10.1002/anie.202400127 From NLM PubMed-not-MEDLINE.

(32) Li, Z.; Tang, M.; Liang, S.; Zhang, M.; Biesold, G. M.; He, Y.; Hao, S.-M.; Choi, W.; Liu, Y.; Peng, J.; et al. Bottlebrush polymers: From controlled synthesis, self-assembly, properties to applications. *Progress in Polymer Science* **2021**, *116*. DOI: 10.1016/j.progpolymsci.2021.101387.
(33) Mansky, P.; Tsui, O. K. C.; Russell, T. P.; Gallot, Y. Phase Coherence and Microphase Separation Transitions in Diblock Copolymer Thin Films. *Macromolecules* **1999**, *32* (15), 4832-4837. DOI: 10.1021/ma990140x.
(34) Müller-Buschbaum, P. GISAXS and GISANS as metrology technique for understanding the 3D morphology of block copolymer thin films. *European Polymer Journal* **2016**, *81*, 470-493. DOI: 10.1016/j.eurpolymj.2016.04.007.
(35) Hexemer, A.; Muller-Buschbaum, P. Advanced grazing-incidence techniques for modern soft-matter materials analysis. *IUCrJ* **2015**, *2* (Pt 1), 106-125. DOI: 10.1107/S2052252514024178 From NLM PubMed-not-MEDLINE.
(36) Dosch, H.; Batterman, B. W.; Wack, D. C. Depth-controlled grazing-incidence diffraction of synchrotron x radiation. *Phys Rev Lett* **1986**, *56* (11), 1144-1147. DOI: 10.1103/PhysRevLett.56.1144 From NLM Publisher.
(37) Hu, M.; Li, X.; Heller, W. T.; Bras, W.; Rzayev, J.; Russell, T. P. Using Grazing-Incidence Small-Angle Neutron Scattering to Study the Orientation of Block Copolymer Morphologies in Thin Films. *Macromolecules* **2023**, *56* (6), 2418-2428. DOI: 10.1021/acs.macromol.2c02415.
(38) https://www.ncnr.nist.gov/resources/activation/.
(39) Alsnielsen, J.; Jacquemain, D.; Kjaer, K.; Leveiller, F.; Lahav, M.; Leiserowitz, L. Principles and applications of grazing incidence X-ray and neutron scattering from ordered molecular monolayers at the air-water interface. *Physics Reports-Review Section of Physics Letters* **1994**, *246* (5), 252-313.
(40) Busch, P.; Rauscher, M.; Smilgies, D.-M.; Posselt, D.; Papadakis, C. M. Grazing-incidence small-angle X-ray scattering from thin polymer films with lamellar structures - the scattering cross section in the distorted-wave Born approximation. *Journal of Applied Crystallography* **2006**, *39* (3), 433-442. DOI: doi:10.1107/S0021889806012337.
(41) Lee, B.; Park, I.; Park, H.; Lo, C.-T.; Chang, Taihyun,; Winans, R. E. Electron density map using multiple scattering in grazing-incidence small-angle X-ray scattering. *Journal of Applied Crystallography* **2007**, *40* (3), 496-504. DOI: doi:10.1107/S0021889807011399.
(42) Busch, P.; Rauscher, M.; Moulin, J.-F.; Muller-Buschbaum, P. Debye-Scherrer rings from block copolymer films with powder-like order. *Journal of Applied Crystallography* **2011**, *44* (2), 370-379. DOI: doi:10.1107/S0021889810053823.
(43) Vineyard, G. H. Grazing-incidence diffraction and the distorted-wave approximation for the study of surfaces. *Physical Review B* **1982**, *26* (8), 4146-4159. DOI: 10.1103/PhysRevB.26.4146.
(44) Sinha, S. K.; Sirota, E. B.; Garoff, S.; Stanley, H. B. X-ray and neutron scattering from rough surfaces. *Physical Review B* **1988**, *38* (4), 2297-2311. DOI: 10.1103/PhysRevB.38.2297.
(45) Rauscher, M.; Salditt, T.; Spohn, H. Small-angle x-ray scattering under grazing incidence: The cross section in the distorted-wave Born approximation. *Physical Review B* **1995**, *52* (23), 16855-16863. DOI: 10.1103/PhysRevB.52.16855.
(46) Rauscher, M.; Paniago, R.; Metzger, H.; Kovats, Z.; Domke, J.; Peisl, J.; Pfannes, H.-D.; Schulze, J.; Eisele, I. Grazing incidence small angle x-ray scattering from free-standing nanostructures. *Journal of Applied Physics* **1999**, *86* (12), 6763-6769. DOI: 10.1063/1.371724 (acccessed 8/20/2025).

(47) Lee, B.; Park, I.; Yoon, J.; Park, S.; Kim, J.; Kim, K.-W.; Chang, T.; Ree, M. Structural Analysis of Block Copolymer Thin Films with Grazing Incidence Small-Angle X-ray Scattering. *Macromolecules* **2005**, *38* (10), 4311-4323. DOI: 10.1021/ma047562d.
(48) Kim, Y. C.; Composto, R. J.; Winey, K. I. pH-Mediated Size-Selective Adsorption of Gold Nanoparticles on Diblock Copolymer Brushes. *ACS Nano* **2023**, *17* (10), 9224-9234. DOI: 10.1021/acsnano.3c00212 From NLM PubMed-not-MEDLINE.
(49) Hu, M.; Gan, X.; Chen, Z.; Seong, H.-G.; Emrick, T.; Russell, T. P. Quantitative X-ray scattering and reflectivity measurements of polymer thin films with 2D detectors. *Journal of Polymer Science* **2024**, *62* (16), 3642-3662. DOI: 10.1002/pol.20230530.
(50) Heller, W. T.; Cuneo, M.; Debeer-Schmitt, L.; Do, C.; He, L.; Heroux, L.; Littrell, K.; Pingali, S. V.; Qian, S.; Stanley, C.; et al. The suite of small-angle neutron scattering instruments at Oak Ridge National LaboratoryThis article will form part of a virtual special issue on advanced neutron scattering instrumentation, marking the 50th anniversary of the journal. *Journal of Applied Crystallography* **2018**, *51* (2), 242-248. DOI: doi:10.1107/S1600576718001231.
(51) Heller, W. T.; Hetrick, J.; Bilheux, J.; Calvo, J. M. B.; Chen, W.-R.; DeBeer-Schmitt, L.; Do, C.; Doucet, M.; Fitzsimmons, M. R.; Godoy, W. F.; et al. drtsans: The data reduction toolkit for small-angle neutron scattering at Oak Ridge National Laboratory. *SoftwareX* **2022**, *19*, 101101. DOI: 10.1016/j.softx.2022.101101.